Unravelling Landslide Failure Mechanisms with Seismic Signal Analysis for Enhanced Pre-Survey Understanding

Jui-Ming Chang[1,2], Che-Ming Yang[3]*, Wei-An Chao[1,2], Chin-Shang Ku[4], Ming-Wan Huang[3,5], Tung-Chou Hsieh[2], Chi-Yao Hung[6]

[1]Department of Civil Engineering, National Yang Ming Chiao Tung University, Hsinchu 30010, Taiwan

[2]Disaster Prevention and Water Environment Research Center, National Yang Ming Chiao Tung University, Hsinchu 30010, Taiwan

[3]Department of Civil and Disaster Prevention Engineering, National United University, Miaoli 36063, Taiwan

[4]Institute of Earth Sciences, Academia Sinica, Taipei 11529, Taiwan

[5]He Yu Engineering Consultants Co. Ltd., Taichung 40642, Taiwan

[6]Department of Soil and Water Conservation, National Chung Hsing University, Taichung 40227, Taiwan

Correspondence to: Che-Ming Yang (stanleyyangcm@nuu.edu.tw)

Abstract

Seismic signals, with their remote and continuous monitoring advantages, have been instrumental in unveiling various landslide characteristics and have been widely applied in the past decades. However, a few studies have extended these results to provide geologists with pre-survey information, thus enhancing the understanding of the landslide process. In this research, we utilize the deep-seated Cilan Landslide (CL) as a case study and employ a series of seismic analyses, including spectrogram analysis, single force inversion, and geohazard location. These techniques enable us to determine the physical processes, sliding direction, mass amount estimation, and location of the deep-seated landslide. Through efficient discrete Fourier transform for spectrograms, we identified three distinct events, with the first being the most substantial. Further analysis of spectrograms using a semi-log frequency axis generated by discrete Stockwell transform revealed that Event 1 consisted of four sliding failures occurring within thirty seconds with decreasing sliding mass. Subsequent Events 2 and 3 were minor toppling and rockfalls, respectively. Geohazard location further constrained the source location, indicating that Events 1 and 2 likely originated from the same slope. Subsequently, the sliding direction retrieved from single force inversion and volume estimation was determined to be 153.67° and 557,118 m^3, respectively, for the CL. Geological survey data with drone analysis corroborated the above seismological findings, with the sliding direction and source volume estimated to be around 148° and 664,926 m^3, respectively, closely aligning with the seismic results. Furthermore, the detailed dynamic process observed in the spectrogram of Event 1 suggested a possible failure mechanism of CL involving advancing, retrogressing, enlarging, or widening. Combining the above mechanism with geomorphological features identified during field surveys, such as the imbrication-like feature in the deposits and the gravitational slope deformation, with event video, infers the failure mechanism of retrogression of the Event 1 after shear-off from the toe. Then, the widening activity was caused by the failure process for subsequent events, as Events 2 and 3. This case study underscores the significance of remote and adjacent seismic stations in offering seismological-based landslide characteristics and a time vision of the physical processes of landslides, thereby assisting geologists in landslide observation and deciphering landslide evolution.

Keywords: Cilan Landslide**,** Spectrograms**,** Discrete Stockwell Transform, Landslide Failure Mechanism

1 Introduction

In recent decades, seismology has expanded in scope to include mass movements on the Earth's surface since the first observation of landslide signals during volcanic eruptions (Kanamori and Given, 1982). After that, the application of associated analyses from seismology, particularly in landslide research has gradually increased (Brodsky et al., 2003; Vilajosana et al., 2008; Feng, 2011; Allstadt et al., 2013; Hibert et al., 2014; Dietze et al., 2017).

Different seismic signal frequencies play distinct roles in landslide characterization. Low-frequency seismic signals, typically below 0.1 Hz, have been employed to approximate the source location, estimate the sliding direction, and reconstruct its trajectory (Yamada et al., 2013; Hibert et al., 2015; Chao et al., 2018). These signals are generated by ground rebound from slope failure, which were detected in the cases of massive landslides with areas greater than 10,000 m^2 or volumes exceeding 100,000 m^3 (Kuo et al., 2018). Moreover, low-frequency signals have unique characteristics that can be used as distinguishing features. The signal source is assumed to be a point source that undergoes loading and unloading processes. By comparing synthetic and observed waveforms from a single force mechanism using a grid search and by adapting data from seismic stations, the approximate source location and inverted force direction of a landslide can be determined (Chao et al., 2017). The magnitude of the inverted force is related to the landslide scale (Ekström and Stark, 2013; Chao et al., 2016). However, because of the longer wavelengths associated with low-frequency signals, the accuracy of the source constraints is reduced compared to higher-frequency signals.

High-frequency seismic signals (>1Hz) have different functions in landslide research. They are, for example, used to recognize the details of the source mechanism (Provost et al., 2018; Weng et al., 2022) and the constraints of the source location (Chen et al., 2013; Walsh et al., 2017; Yang et al., 2022). Seismic time-frequency spectrograms have been identified as the source type. Compared with the right triangle spectrogram feature associated with the onset of the P-wave of earthquakes, landslides typically exhibit a cigar-shaped feature with a linear (Suriñach et al., 2005; Moretti et al., 2012) or semi-log (Dammeier et al., 2011) frequency axis resulting from the Fourier transform. More recently, other spectrogram features, such as V-shaped, column-shaped, and pulse-like features corresponding to the

70 failure mechanisms of sliding, toppling, and rockfall, respectively (Chang et al., 2021) have been observed

71 in spectrograms generated by the Stockwell transform with a semi-log plot. However, the advantages and

72 disadvantages of these two linear and semi-log label transforms have not been thoroughly addressed.

73 Through spectrogram recognition, the duration of the physical processes of a landslide can be determined.

74   There are three methods used for the source location: (1) time difference (Chen et al., 2013; Fuchs

75 et al., 2018; Manconi and Mondini, 2022), (2) amplitude decay (Aki and Ferrazzini, 2000; Walter et al.,

76 2017), and (3) the azimuth of polarization analysis (Guinau et al., 2019). The time-difference method

77 calculates the time difference between pairs of stations using a velocity model to constrain possible source

78 locations. The accuracy of location determination depends upon the station coverage of the source area

79 (Chang et al., 2023). The amplitude source location method considers the decay of the seismic amplitude

80 with distance. However, the results can be influenced by the distribution of the source-station distances,

81 which often leads to the source location being biased toward the station with the highest amplitude caused

82 by site effect (Chang et al., 2023). Although the first and second methods are commonly used in landslide

83 research, the azimuth of polarization analysis has rarely been discussed in landslide source analysis.

84 Guinau et al. (2019) adapted the polarization to retrieve the source azimuth and locate the rockfall by

85 recognizing P- and S-waves through particle motion.

86   Investigations into low- and high-frequency seismic signals provide invaluable perspectives on

87 landslides. However, few studies have sorted out the information as preliminary knowledge to geologists,

88 especially for the continuous time vision of the failure process. Historically, geologists relied solely on

89 field and drone surveys conducted before and after landslide events to depict landslide failure mechanisms,

90 thereby lacking associated information on temporal evolution to link different phases of landslide activity.

91 Geologists need to speculate on the connection of landslide activity to the geological model. However,

92 seismological-based information complements this approach by providing temporal context. Therefore,

93 this study integrates seismic results with landslide investigation (field and drone surveys) to illustrate

94 constructing a landslide evolution model.

95

2 Background information

2.1 Landslides During Typhoon Nesat

Torrential rainfall resulting from the interaction between Typhoon Nesat and the winter monsoon lashed Yilan County in northeast Taiwan from 15 October to 17 October 2022 (Fig. 1a; the time in this research all shows in local time UTC+8). The accumulated precipitation reached 1,000 mm in three days, with a peak rainfall intensity of 103 mm hr^{-1}. (Fig. 1b). This accumulation exceeded the landslide threshold of 550 mm, as documented by the Agency of Rural Development and Soil and Water Conservation (https://246.ardswc.gov.tw/; last accessed on 30 October 2024). Consequently, many rainfall-induced landslides occurred. Most landslides accumulated next to roads (Fig. S1), destroying sections of two vital provincial highways: No. 7 (Northern Cross-Island Highway) and No. 7A (Fig. 1a). The Directorate General of Highways, Taiwan, reported nine sections damaged by landslides (Figs. 1c-1j; Table S1). Among these, three roadbed washouts characterized by argillite/slate were observed in the Paling Formation (Figs. 1c-1e), whereas a landslide composed of slate covered a road section in the Lushan Formation (Fig. 1f). Additionally, four debris flow events occurred near the boundary between the Lushan Formation and the alluvium (Figs. 1g-1j). As of 22 October 2022, these events left 302 people stranded, resulting in one missing person. In addition to these nine events, a deep-seated landslide, known as the Cilan landslide (CL), occurred in the Lushan Formation. Initially, an individual captured a part of the CL process on video, revealing two distinct stages of material sliding (Fig. S2). According to the video footage, the initial landslide was formed by exposure to the bare earth. The video captured the subsequent failures. The first body in the footage slid between 0-20 seconds, and the following failure occurred at the 20-second mark in the video recording. Then, the Directorate General of Highways in Taiwan identified the precise location of the landslide (Fig. S3 and yellow star in Fig. 1a) and provided an approximate occurrence time of 4:00 PM on 16 October 2022.

119
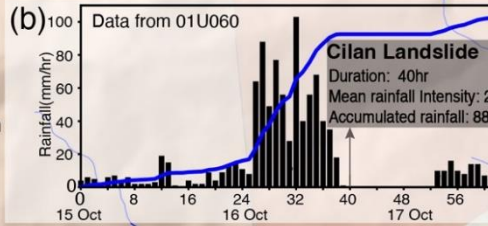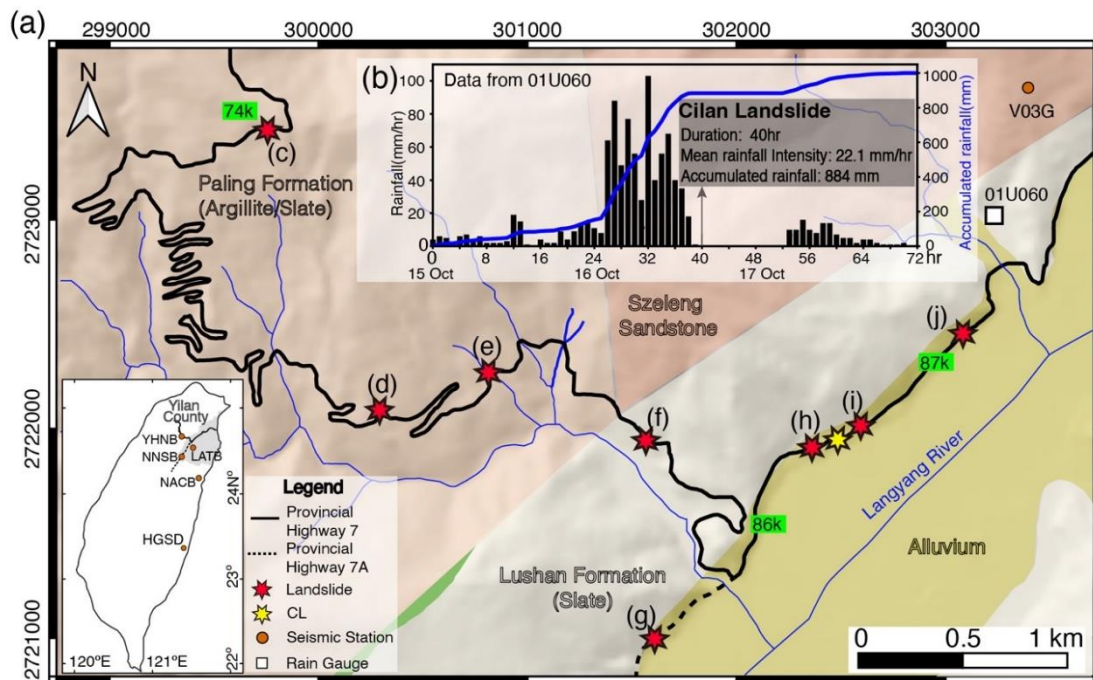
Figure 1 (a) Regional geologic map of roadside landslides, seismic station, and rain gauge (Fei and Chen, 2013). The grey-shaded area in the map of Taiwan (lower left) represents Yilan County. (b) Rainfall data of rain gauge 01U060 during the typhoon. The rain episode started on 15 October 2022 at 00:00 AM (Local time UTC+8). (c)-(j) In situ photos for landslides. All photos are open data from the Directorate General of Highways, Taiwan (Table S1). The k in the map/photos indicates the milestone (in kilometers) of two provincial highways.

2.2 Topographic Feature Near the CL

According to 1-m high-resolution LiDAR-derived slope inclination map (Fig. 2), several prominent features were evident near the CL. On the west side of the CL, a concave slope displayed distinct scarps and gullies. These features strongly indicated that the concave slope was subject to erosion. Conversely, the eastern roadside slopes of the CL revealed a contrasting topography characterized by numerous scarplets with several gullies and convex slopes, all prone to rockfalls. Within this context, slopes at the 86.5 km and 86.7 km milestones along Provincial Highway No. 7 experienced a debris flow on the gentler portions (Fig. 1h) and talus deposits on the steeper sections (Fig. 1i).
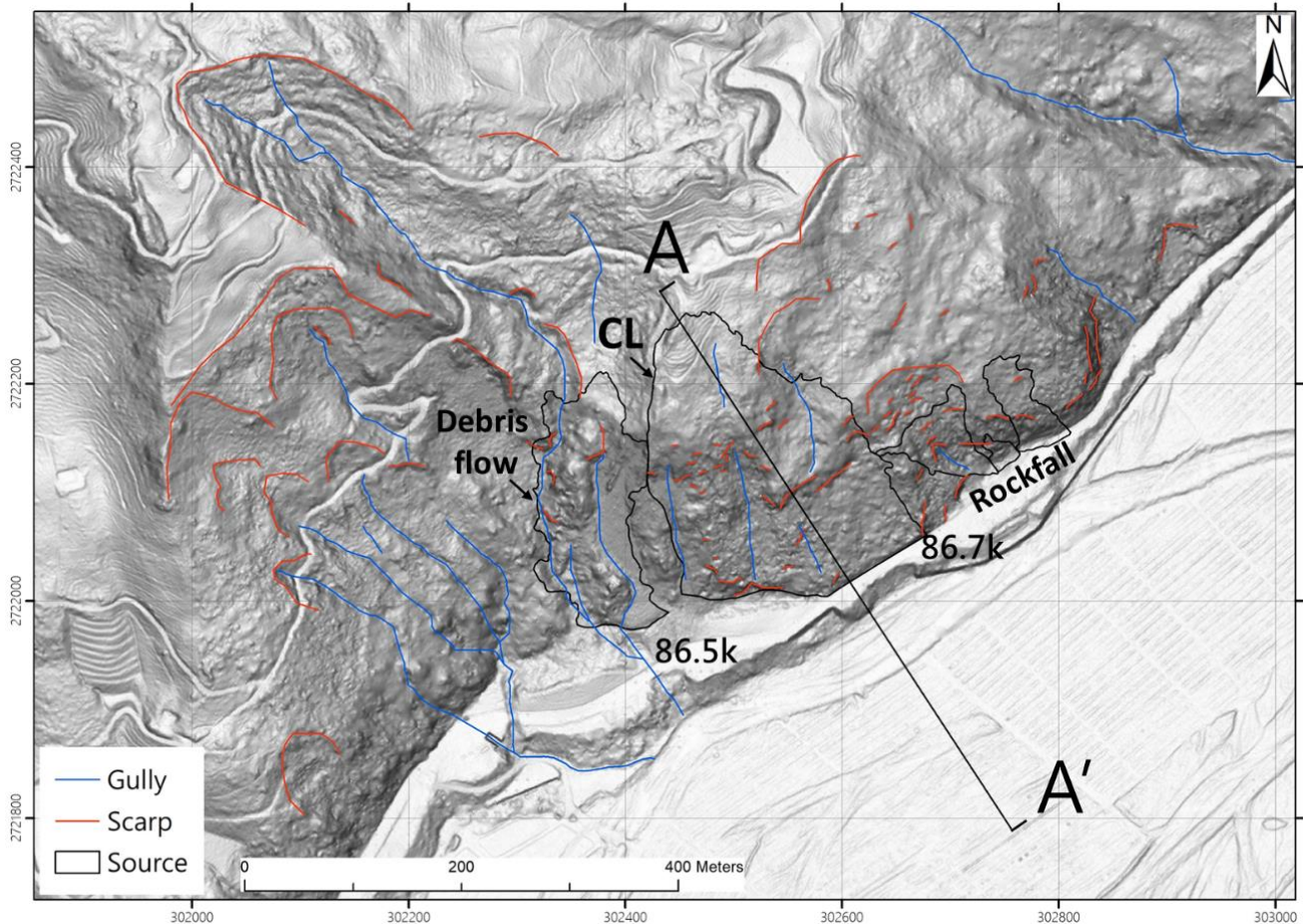
Figure 2 Topographic feature interpretation with 1 m high-resolution LiDAR slope map in 2014 before the CL. The AA' is for the topographic profile in Fig. 7b. The black line polygons indicate the source boundary of slope failures.

3. Methods

The study aims to leverage seismic analysis as preliminary knowledge to aid in illustrating the landslide evolution model of the CL. To achieve this, we conducted a series of seismic signal analyses, including seismic signal spectrograms, single force inversion (SF), and geohazard location (GeoLoc). These analyses provide insights into the temporal evolution of the failure process, landslide magnitude, inverted force direction, and landslide location constraints. Geologists use these results to gain a basic understanding of the CL prior to conducting a field survey. The field survey consists of two parts: geological investigation and drone survey. The former provides geological background information, while the latter, joining LiDAR in 2014, captures topographic features and changes post-CL. The combined results from the seismic signal analyses and field surveys support the development of the most plausible landslide evolution model. The flowchart is depicted in Fig. 3.
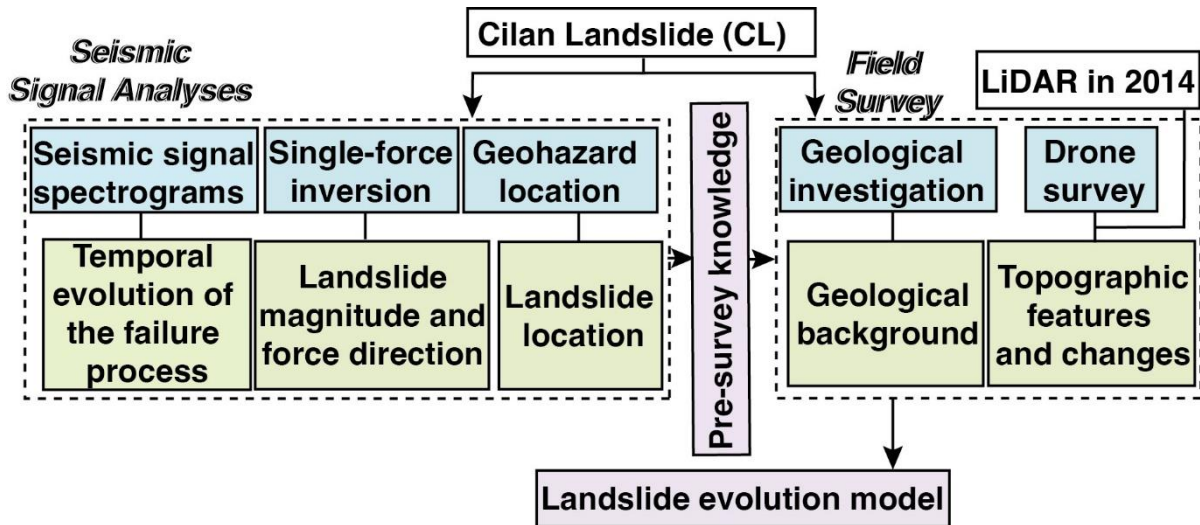
Figure 3 Flowchart of this study. The blue, green, and purple backgrounds are relevant to the methodology, results, and discussion.

3.1 Seismic signal spectrograms

The study investigated time-frequency spectrograms based on the power spectral density (PSD) of the discrete Fourier transform (DFT), as well as the power spectrum (PS) of the discrete Stockwell transform (DST). The DST of Eq. (1) was derived from Eq. (2), while f, τ, t, and α were derived from Eqs. (3)-(7).

$$DST:\ s[p\Delta t, \tfrac{l}{N\Delta t}] = \sum_{m=1}^{N-1} \quad H[\tfrac{l+m}{N\Delta t}]e^{-2\pi^2 \frac{m^2}{l^2}} e^{2\pi i \frac{mp}{N}} \tag{1}$$

$$DFT:\ H[\tfrac{l}{N\Delta t}] = \tfrac{1}{N}\sum_{k=0}^{N-1} \quad h[k\Delta t]e^{-2\pi i \frac{lk}{N}} \tag{2}$$

$$f = \tfrac{l}{N\Delta t} \ , l = 0,1,2 \ldots N-1 \tag{3}$$

$$\tau = p\Delta t \ , p = 0,1,2 \ldots N-1 \tag{4}$$

$$\alpha = \tfrac{m}{N\Delta t} \ , m = 0,1,2 \ldots N-1 \tag{5}$$

$$t = k\Delta t \ , k = 0,1,2 \ldots N-1 \tag{6}$$

$$PS = s[p\Delta t, \tfrac{l}{N\Delta t}]^2 \tag{7}$$

where Δt is the time sample interval, τ denotes the time of spectral localization, N is the total number of data points, α, and f control the discrete frequency point, and $h[t]$ is the discrete-time series seismic data.

In the context of landslides, the predominant frequencies of ground vibrations typically range from 1 Hz to 10 Hz (Chang et al., 2021). To represent the power distribution within this range precisely, we configured the DFT analysis to have time and frequency resolutions of 1.28 seconds and 0.39 Hz, respectively. This configuration effectively captured the pertinent frequency information while retaining an acceptable time resolution. Also, a cumulative PSD plot was obtained by summing the PSD values at discrete time intervals. Alternately, applying DST instead of DFT allows for either enhanced frequency resolution for the lower frequencies through broader time windows or improved time resolution for the higher frequencies through narrower windows. In this study, we opted for a time window of 0.05 seconds and a frequency resolution of 0.30 Hz in the DST analysis. These parameters provided superior frequency and time resolutions, enabling the capture of intricate spectrogram details.

177   The scale of the frequency axis on the spectrograms profoundly influences recognition and
178 interpretation within the target frequency range of 1 Hz to 10 Hz. Therefore, we incorporated linear and
179 logarithmic frequency axes into the spectrograms. By judiciously selecting window lengths, time and
180 frequency resolutions, and frequency axes, we facilitated effective visualization and analysis of the power
181 distribution in seismic signals, particularly within the frequency range pertinent to landslide occurrences.

182 **3.2 Single-force inversion (SF)**

183   Single-force inversion (SF) is a technique used in the near-real-time landquake monitoring system
184 (NRLAMS) to extract the possible force direction and magnitude of a landslide (Chao et al., 2017; Chang
185 et al., 2024). Before conducting the SF analysis, we performed several preprocessing steps on the seismic
186 signals. First, we applied a bandpass filter between 0.02 Hz and 0.05 Hz to isolate the frequency range
187 for large-scale landslides (volume $> 10^5 \, \text{m}^3$ or area $> 10^4 \, \text{m}^2$, as defined by Chen, 2015). This frequency
188 range is associated with landslide-related signals in Taiwan (Chao et al., 2017). In addition, we
189 transformed the original horizontal components of the seismic data into radial and tangential components.
190 Different weightings in the SF correspond to the signal-to-noise ratio (SNR) (Table S2), the ratio between
191 the absolute peak amplitude and the average absolute amplitude from the entire signal trace.

192   Subsequently, the SF analysis simulated synthetic waveforms assuming a source depth of 1 km,
193 and Green's functions were calculated based on the surface wave velocity model proposed by Shin and
194 Chen (1998). Different synthetic waveforms were generated using different settings of force direction,
195 magnitudes, and dips. These waveforms were compared with the observed signals regarding fitness values,
196 the sum of the maximum normalized cross-correlation coefficient, and variance reduction. The highest
197 fitness values corresponding to the inverted force parameters were determined. Furthermore, a parameter
198 of inverted force magnitude (unit: Newton) of SF could be used to estimate the landslide mass through
199 the empirical formula, mass (kg) = 0.405 × force magnitude (Chao et al., 2016). Assuming a rock density
200 of approximately 2,600 kg m^{-3}, the estimated landslide mass could be roughly converted to landslide
201 volume. The seismic data for the SF analysis were obtained from a broadband array in Taiwan for seismic
202 networks (Kao et al., 1998). A more detailed methodology associated with the parameter setting and
203 procedure is provided by Chao et al. (2017).

3.3 Geohazard location

The geohazard location (GeoLoc) method, as outlined by Chang et al. (2021), synergizes the cross-correlation (CC) method (Chen et al., 2013) with the amplitude source location (ASL) method (Aki and Ferrazzin, 2000) to pinpoint potential landslide locations using seismic signals in the frequency range of over 1 Hz. This approach initially filtered the seismic data between 1 Hz and 3 Hz. Subsequently, the SNR was calculated as a ratio between the short-term average ($\pm$ 5 s from the maximum envelope amplitude) and the long-term average of a 180-second target trace. A threshold of SNR larger than 1.7 was applied to select the available waveforms for further analysis. The selected frequency range and SNR threshold were empirically established based on extensive-scale landslides in Taiwan (Chen et al., 2013).

The CC method calculates the maximum cross-correlation coefficient between each station pair to extract the travel time difference. This difference was then used with a three-dimensional velocity model (Wu et al., 2007) and grid search to define the misfit function. Simultaneously, the ASL method gauges its misfit function by optimizing the fit of the amplitude decay curve. By individually sorting the misfit functions across all search grids, both methodologies yielded reliable source locations for landslides. The potential source locations were identified when the grids had relative fitness values greater than 0.95 Chang et al. (2023). The detailed algorithm of GeoLoc can be found in Chang et al. (2021).

Seismic data for GeoLoc analysis were collected from various sources (Table S3), including temporary stations maintained by the Comprehensive Landquake Monitoring Lab (CoLLab), National Yang Ming Chiao Tung University, a broadband array in Taiwan for seismology, and the Central Weather Administration, Taiwan.

3.4 Field survey

The field survey encompassed two integral components: drone survey and geological investigation on 19 October 2022. For the drone survey, we conducted a series of vertical and inclined aerial photos along the CL using the DJI Phantom 4. These photos were input for the photogrammetry software Pix4D, which generated a digital surface model (DSM). Through the DSM, the geomorphological features after the CL could be depicted. Additionally, by combining the LiDAR data

from 2014 with digital elevation model (DEM), we could observe the differences in topography before and after the CL event. The LiDAR DEM was obtained from the Ministry of the Interior, Taiwan. The drone-derived DSM was produced using ground control points via the e-GNSS service (Virtual Reference Station Real-Time Kinematic technology) provided by the Ministry of the Interior, Taiwan. The vertical root mean square errors for the LiDAR DEM and the drone-derived DSM were found to be 0.5 m and 0.2 m, respectively. On the other hand, the geological investigation focused on road inspection and outcrop observation before and after the CL, respectively. The road inspection documented the status of slope protection, particularly regarding crack geometry. The outcrop observation recorded the strike and dip for cleavage, joints, and bedding near the CL.

4. Result

4.1 Seismic spectrograms for the CL

According to the one-hour spectrogram generated through DFT analysis of V03G (Fig. 4a), the resulting spectrograms revealed three distinct high-power onsets potentially corresponding to different landslide events. The first event, labeled Event 1, occurred from 16:10:00 to 16:10:30. The cigar-shaped features of the spectrograms indicated a landslide process when the spectrograms were analyzed using a linear frequency axis (Fig. 4b). However, when the DST was modified to a semi-log graph, the lower bounds of the high PSD displayed V-shaped spectrogram features (Fig. 4c). Such V-shaped patterns were not discernible in the spectrograms obtained using the DFT because of the inherent limitations imposed by the frequency and time resolution (Fig. 4b). The V-shape is associated with sliding behavior (Chang et al., 2021), which involves phases of acceleration and deceleration of the landslide materials separated by the lowest point of the V-shape. In Event 1, the four V-shaped events were interconnected, and their lowest points (depicted as purple dots in Fig. 4c) gradually shifted to higher frequencies, indicating a reduction in the sliding material volume. The clear and consistent pattern indicates that the signals are most likely from a single landslide event. As a result, the event was the initial sliding of massive mass, which also generated signals within the frequency range of 0.02 Hz to 0.05 Hz, detectable by the SF method (See following subsection). With smaller volumes involved in the subsequent sliding events, the corresponding signals in the low-frequency range could not be generated.

Approximately 20 min after Event 1, Event 2 occurred, and the spectrogram revealed a sequence of continuous pulse-like features (black rectangle in Fig. 4d). However, the frequency bands associated with these pulse-like features overlapped with ambient noise. Certain pulse-like features could be discerned, indicating continuous rock-ground impacts in the form of rockfalls. Subsequently, a column-like shape emerged in the spectrogram, an interaction between the substantial mass and the slope or ground (dashed black rectangle in Fig. 4d). This phenomenon referred to processes such as toppling or rockfalls on overhanging slopes or similar mechanisms. Approximately 26 min later, Event 3 emerged, presenting spectrogram features analogous to the continuous rock-ground impacts observed in Event 2 (black rectangle in Fig. 4e). In particular, a gradual decrease in the PSD and PS values and signal durations was evident from Events 1 to 3, presenting a reduction in the scale of the landslide.
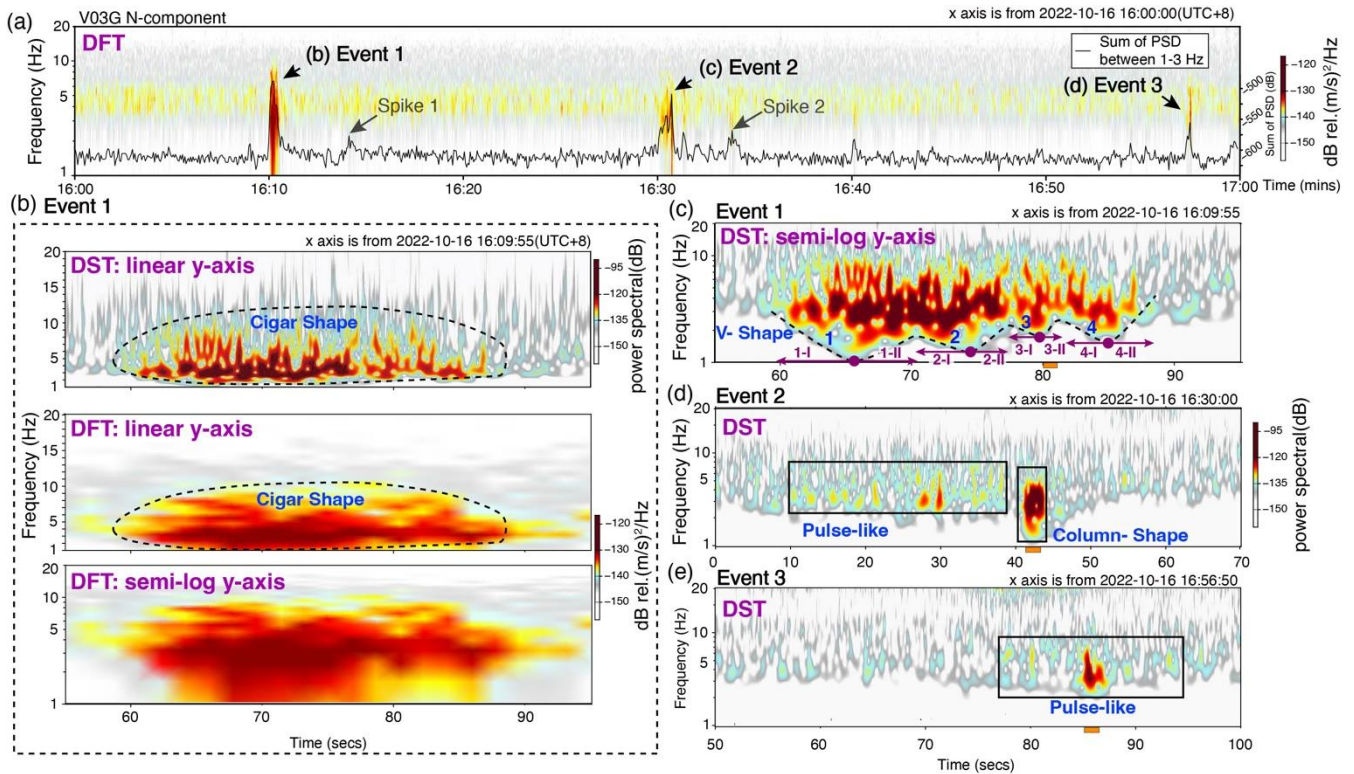
Figure 4 Spectrograms of the seismic signal from V03G with the North component. (a) DFT spectrogram and PSD sum between 16:00-17:00 on 16 October 2022 (UTC+8). (b) Event 1 of DST with linear frequency axis and DFT with linear frequency and semi-log frequency axes. (c) DST spectrogram with

271   semi-log frequency axes for Event 1. The black dashed line is the lower boundary of the high PS values,

272   showing the V-shaped spectrogram feature. The purple points are the lowest points of the four V-shapes

273   that separate the first half (I), the acceleration phase, from the second half (II), the deceleration phase.

274   The blue numbers indicate a sequence of the V-shapes. (d) Spectrogram of DST for Event 2. The black

275   rectangles mark the spectrogram feature. (e) DST spectrogram for Event 3. The horizontal orange bars

276   below the x-axis in (c)(d)(e) are the signal windows for particle motion analysis in Fig. 10.

277   Except for Events 1 to 3, Fig. 4a exhibited two spikes. We examined the corresponding

278   spectrograms and found that the signals were faint and heavily obscured by ambient noise (Fig. S4).

279   Consequently, the evidence derived from these indirect observations does not substantiate their origin

280   from landslide activity.

281   **4.2 Single-force inversion for the CL**

282   We employed an SF approach for Event 1 of the CL, utilizing a network of five seismic stations

283   (Fig. 5a). Source-station distances spanned from 7.80 km to 124.13 km, and back azimuths ranged from

284   170º to 296º. After testing several starting times of the seismic signals for the SF, we found that signals

285   starting at 16:10:04 yielded the best results. The normalized cross-correlation coefficient and the variance

286   reduction of these signals averaged 0.72 and 0.74, respectively (Fig. 5b). The overall performance

287   exhibited a fitness value 1.08. Subsequently, the SNR values ranged from 2.93 to 6.00, and the NACB

288   consistently exhibited a relatively high SNR across the three components. The inversion process yielded

289   a force direction of $153.67°$ and a force magnitude of 3.36×10^9 (Newton). The magnitude of the force was

290   converted into landslide mass using an empirical formula, and the landslide volume was estimated to be

291   approximately 523,540 m^3.
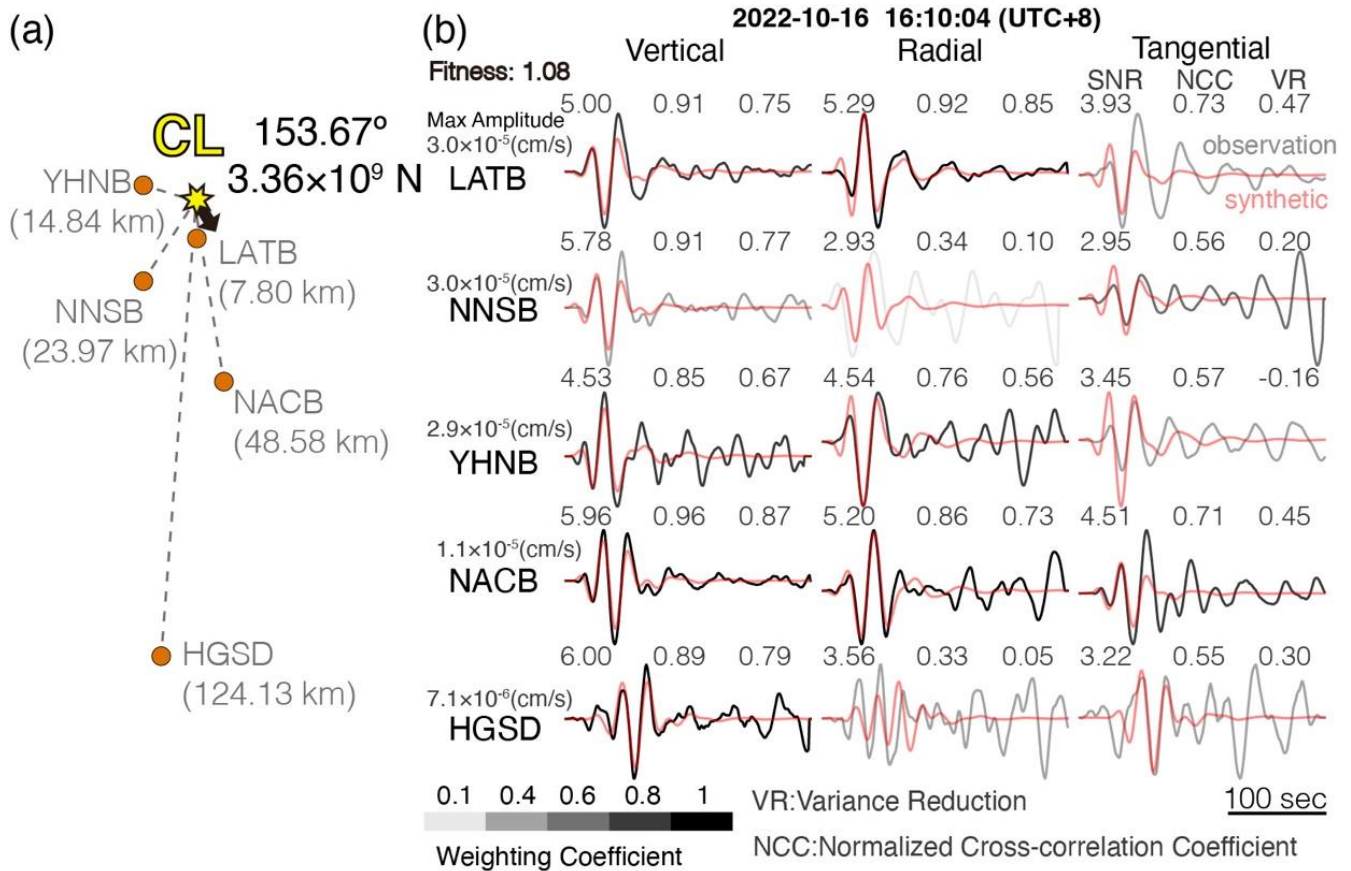
Figure 5 (a) Position of seismic stations relative to the CL. The black arrow indicates the inverted force direction of 153.67° with a force magnitude of 3.36×10^9 (Newton). (b) Synthetic and observation waveforms of the CL with SNR, normalized cross-correlation coefficient, and variance reduction. The grey gradient presents the different weightings to retrieve the fitness corresponding to the SNR of the signals (Table S2).

4.3 Source location

The V03G station recorded Events 1 to 3. Assuming these signals originated from the same slope of landslides, the characteristics of the spectrogram could provide valuable insights into the short-term behavior of the CL. Therefore, to determine the locations of Events 1 to 3, we utilized the GeoLoc method. The results of Events 1 and 2 of the CC, considering both the horizontal and vertical components, indicated that the grids with high fitness values (> 0.95) were close to the V03G station (Purple grid cells in Fig. 6). In addition, the ASL tended to be near the station with the highest amplitude (Fig. S5).

Therefore, Events 1 and 2 probably originated from the same landslide location. For Event 3, the signals were too weak to be detected by the ENT and LATB stations. Only V03G recorded its signals, which supports the location of Event 3 near the V03G station.
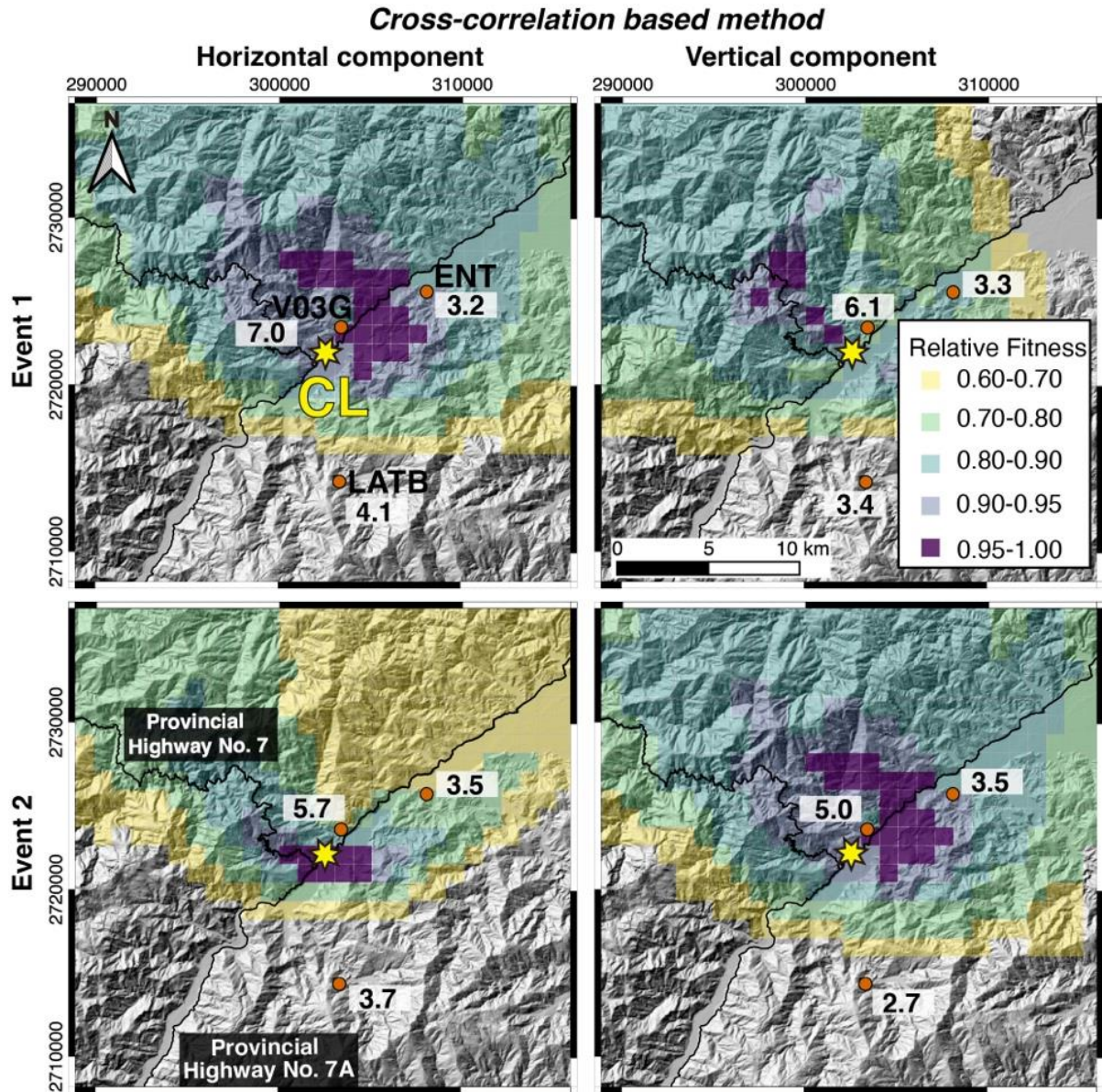
Figure 6 Location determination by cross-correlation-based method of horizontal and vertical component data for Event 1 and Event 2. The values following the stations with transparent white backgrounds are SNR.

4.4 Landslide survey

According to the topographic profile (A-A' in Fig. 7a), the sliding direction was approximately 148°, similar to the result obtained from the SF (153.67°). The observed elevation difference and travel distance of the CL were 220 m and 530 m, respectively. The apparent friction angle ranged from 22° to 31°, transitioning from the main scarp to the first significant and subsequent failures (Fig. 7b). This variation could be attributed to the depositional environments and landslide volumes.

Furthermore, we compared the topographical profiles before (1m high-resolution LiDAR data in 2014) and after (drone-derived DSM) the CL. The data revealed that the maximum erosion depth approached approximately 45 m near the left flank of the CL, where the bedrock was exposed. For the location, photographic evidence shows that the dips of slate cleavage exhibited a gradual transition from steep (at the top) to gentle (at the bottom) (Fig. 7b). This characteristic indicated gravitational slope deformation (Chigira, 1992; Agliardi et al., 2001), suggesting a weakening of the structural integrity and strength of the rock mass constituting the slope. The CL originated from a source area measuring 44,562 m^2 and was deposited over an area of 94,396 m^2, resulting in a maximum colluvium thickness of 30 m (Fig. 7b). The calculated source volume by difference of elevation was approximately 664,926 m^3. Consequently, the landslide mass was converted into a deposited volume of 690,445 m^3.

The slope map of DSM exhibited deposits with imbrication-like features at the landslide toe, which was covered on the wider and flatter colluvium with the first toe. This pattern was contributed to by the widespread colluvium area where numerous trees rest on the colluvium, composed of slate boulders, debris, saprolites, and soils (Figs. 7b and 8). The inclined trees on the colluvium imply the colluvium is displaced with slight disturbance due to the low-friction basal detachment. The imbricated deposits near the original roadside slope represented a depositional sequence resulting from later failures. The result of the geological investigation shows that the dip direction of the slate cleavage corresponded to the slope aspect and sliding direction, with a high dip angle influencing CL failure (Fig. 7b). Additionally, before the occurrence of the CL, an inspection conducted in May 2022 revealed slight damage and displacement of the downslope concrete wall near the slope (Figs. 9a-9e). These damage signs served as early indicators of creeping slope.
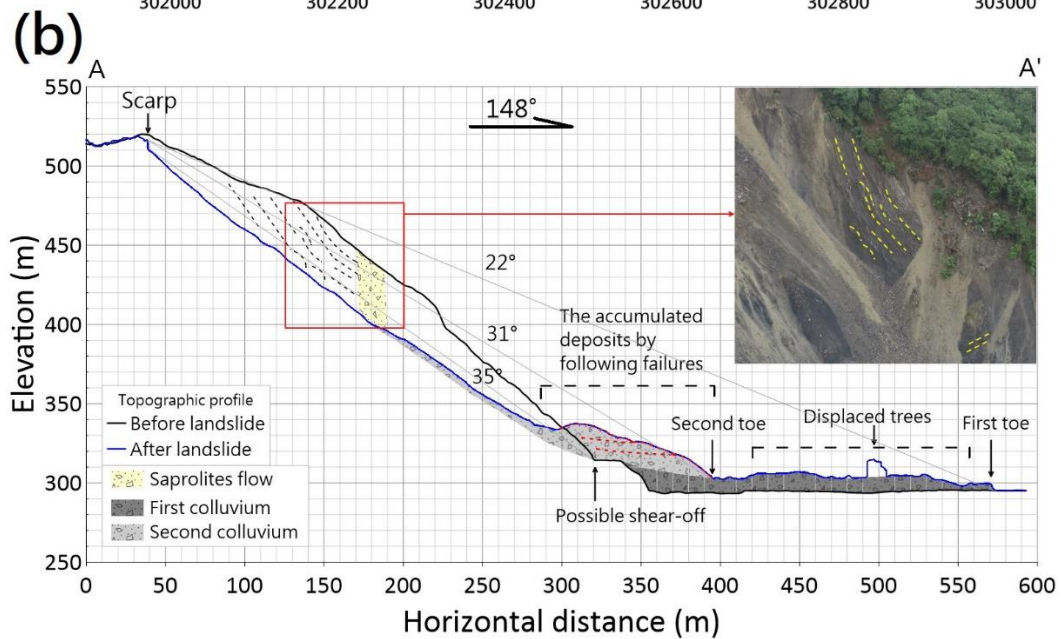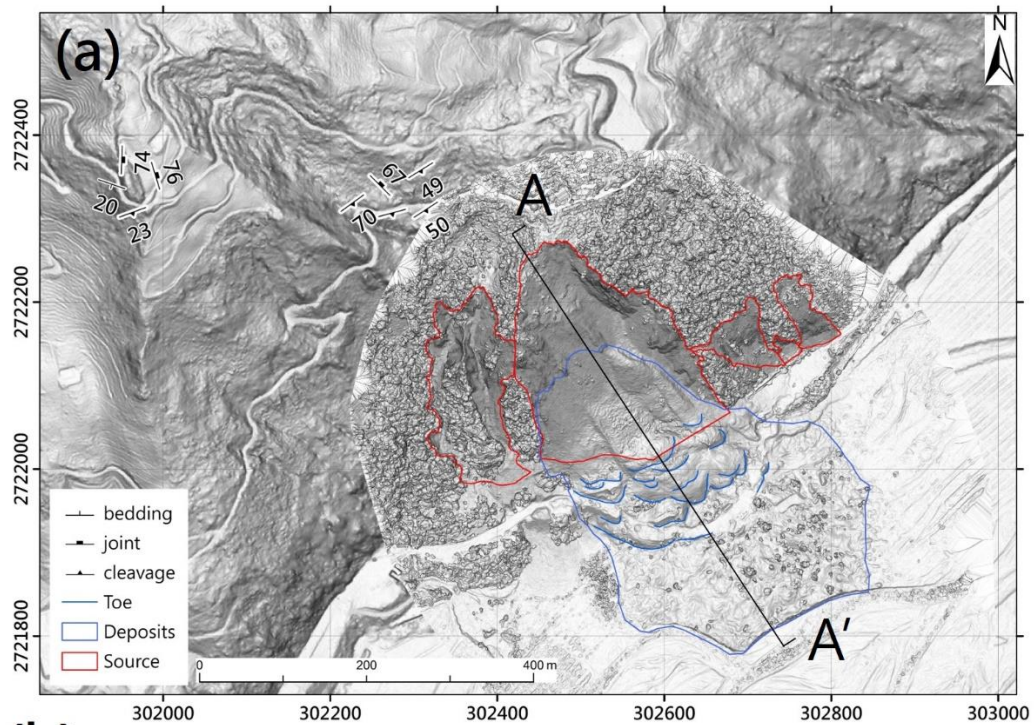
Figure 7 (a) Topographic feature interpretation on drone-based slope map after landslide (19 October 2022). (b) Topographic profile of AA'. The embedded drone photos show the slate outcrop on the left flank of the landslide. The dashed curves indicate that the dip angle and traces of cleavages changed and deformed.

344
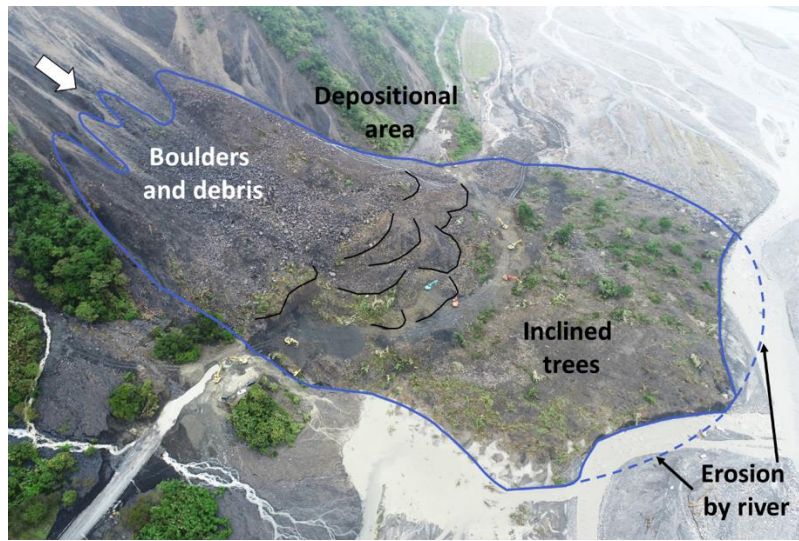
Figure 8 The closed aerial photo of CL deposits. The imbrication-like features are lineated by black lines. The first toe was eroded by river.

347

Figure 9 (a) Google Earth image before the CL. (b)-(e) Photos from inspection on 27 May 2022. (f) Drone-based 3-dimensional model after the CL. (g)-(j) Photos of crown cracks of the CL.

5. Discussion

5.1 Source location of landslide signals

Assuming that Event 1 to Event 3 originated from the slope of the CL, we performed a particle motion analysis within 1 Hz to 3 Hz of V03G (back azimuth: 208°) to clarify their source locations. Given the surface behavior of the landslides, our analysis focused on the vertical and radial components associated with the propagation of Rayleigh waves. Regarding Event 1, we observed intricate patterns of particle motion, particularly during phase 1 of the sliding (Fig. S6). While the initial sliding phase of Event 1 indicated significant movement, the event was governed by a single force mechanism. However, not all materials involved in the landslide exhibited pure shear sliding. Some materials were bouncing, rolling, or interacting with the ground, slopes, and adjacent particles. These physical processes could generate high-frequency signals, resulting in complex and inexplicable particle motion patterns from phase 1 to phase 2 of Event 1. In contrast, the particle motion displayed a more consistent direction during the small-scale mass movement observed in phases 3 and 4, which manifested as clear ellipses. Notably, the ellipse corresponding to phase 3-II of Event 1 was particularly pronounced and linked to Events 2 and 3 (Fig. 10). These elliptical patterns indicated retrograde motion along the travel direction.

Further, we investigated the relationship between different back azimuths and elliptical shapes. When the back azimuth was set at 228°, the elliptical shapes showed a noticeable change (Fig. S7a). However, similar elliptical shapes were consistently observed for back azimuth values ranging from 188° to 148° (Figs. S7b-c). This suggests that elliptical shapes do not exhibit significant sensitivity within 208° to 148°, where sources could potentially originate from a wide back azimuth range. Nevertheless, no documented landslides are reported during the range of back azimuth between 208° to 148° (Fig. S8); most substantial landslides are oriented with back azimuth angles greater than 228° (Fig. 2). Subsequently, the CC and ASL results indicated that Event 2 is close to V03G. Therefore, we posit that at least Event 1 and Event 2 likely originated from the same source direction. Event 3, the minor event, challenges determining its precise location by seismic analysis.
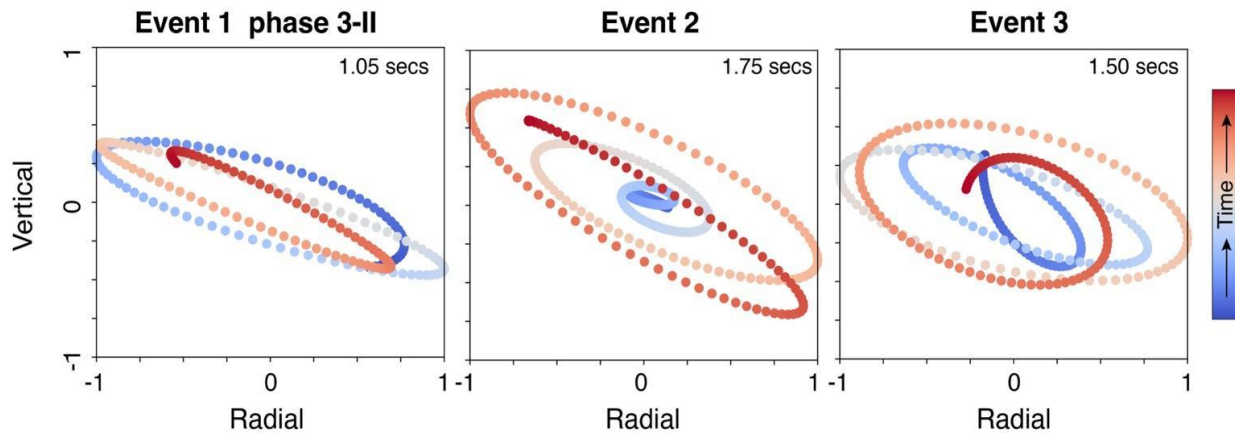
375

376 Figure 10 Particle motion comparison between radial and vertical components for phase 3-II of Event 1,
377 Event 2, and Event 3. The duration of particle motion signals is indicated in the upper right corner of each
378 subfigure, with precise timing details highlighted by orange bars in Fig.4.

379 **5.2 Comprehensive information from seismic analysis**

380   When Event 1 and Event 2 occurred on the same slope, we estimated the approximate volume of
381 the CL using empirical regressions. Event 1 indicated a volume of 523,540 m^3 based on empirical
382 regression (mass = 0.405 × force magnitude; Chao et al., 2016) for large-scale landslides with a sliding
383 direction of 153.67° (Table 1). By retrieving the amplitude at the source (A_0; unit: cm s^{-1}) through 1-8 Hz
384 of horizontal signals, we estimated the volume of Event 2 is 16,791 m^3 (Volume= 77,290 $A_0^{0.44}$; Chang
385 et al., 2021). The total volume obtained from a seismic analysis output of 540,331 m^3 is around 19%
386 lower than the volume estimated by the difference between LiDAR and DSM.

387   Seismic signal analysis provides valuable insight into potential landslide processes. The SF
388 method detailed the timing and movement direction. The DST spectrogram analysis revealed distinct
389 timeframes and physical patterns of the three events associated with slope failure. Event 1 likely involved
390 four sliding failures within 30 seconds with gradually decreasing masses. However, the landslide video
391 captured the process, lasting approximately 34 seconds for probable phases 2 and 3 in Event 1. This
392 discrepancy in timing may be attributed to the weak kinetic energy during the early and termination stages
393 of the CL. The ground vibration signal at those stages might not transmit to V03G, potentially influencing

394 the recorded duration. Subsequently, Event 2 featured 30s of continuous rockfall, followed by a toppling

395 event with a larger mass.

Table 1 Pre-survey information of the CL by seismic analysis

Landslide characteristics	Information	
	Event 1	Event 2
Occurrence time	4:10 PM on 16 October 2022.	4:30 PM on 16 October 2022
Estimated volume	523,540 m^3	16,791 m^3
Sliding direction	153.67º	-
Failure process	Four continuous sliding with the gradual reduction in sliding volume	Rockfall and toppling

397

5.3 Landslide evolution model

399 Landslides are categorized into seven movement types (Varnes, 1978). According to the

400 spectrogram features of Event 1 in the CL, this seismic analysis preferred sliding movement. The stepwise

401 failure process of a landslide can be determined based on the distribution of landslide activity, such as

402 advancing, retrogressive, enlarging, or widening activities (Fig. 11) (WP/WLI, 1993). Advancing and

403 retrogressive activity involves the expansion of the rupture surface along and in the opposite direction of

404 movement. Enlargement entails the rupture surface expanding in multiple directions, whereas widening

405 indices that the rupture surface extends into one or both flanks of the landslide.
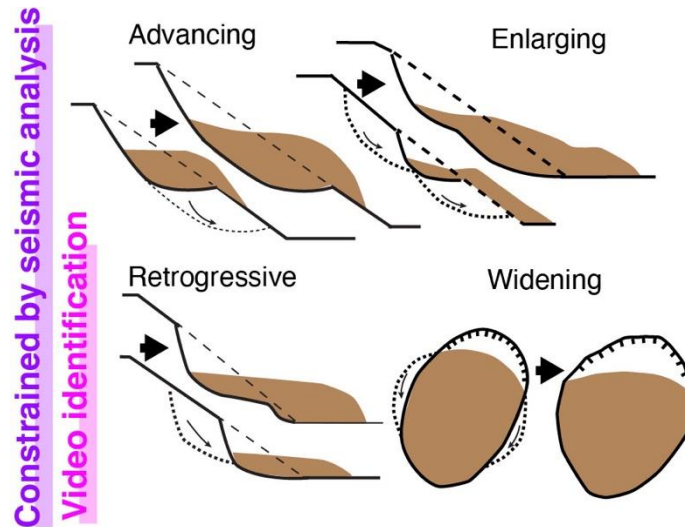
406

407 Figure 11 Schematic diagram of potential landslide activities for the CL. Dot lines represent the
408 detachments in the next stage. Dash lines indicate the original ground level. The brown color indicates
409 the extent of displaced material. The figure has been modified from Cooper (2007).

410 For the CL, the left flank was exposed at the beginning of the video (Fig. S2), which implies
411 previous failures had occurred earlier than the beginning of the video. It is reasonable that people were
412 attracted by previous failures and prepared to take videos for subsequent failures. Besides, the debris flow
413 had deposited a debris fan on the road (Fig. 2h), and excavators were operated to clear the buried road
414 section. The moving mass from the upslope was sliding downward and pushing the previous colluvium.
415 Moreover, some trees displaced to downslope on the top of moving mass, which implies a similar
416 phenomenon during early failure with similar landslide source conditions (Fig. 7). Consequently, the
417 video recorded the process of sliding that could correspond to the distribution and geometry of deposits
418 (Figs. 7 and 8) and validate the sliding of Event 1 by seismic analysis (Fig. 4d).

419 Combining the pre-survey understanding with the survey results, the initial model for landslide
420 evolution was established (Fig. 12a). According to the announces of the Directorate General of Highways
421 in Taiwan (Table S1) and the CL occurrence time extracted by seismic analysis, the debris flow and
422 rockfall were induced by heavy rainfall before the CL (Fig. 12b). The initial failure mechanism of the CL
423 could be assumed to initiate at a shear-off from the original toe (roadside slope) caused by the high pore-
424 water pressure after heavy rainfall infiltration. The first failure should deposit on sandy and gravelly

alluvial deposits with high water levels (Fig. 12b). The rapid loading of sliding mass onto the wet alluvial deposits may have induced liquefaction and reduced the basal friction of sliding mass (Sassa, 1992). The first failure had the most significant volume, leading to higher mobility (Figs. 7, 8, and 12c) (Corominus, 1996; Legros, 2002; Hungr and Evans, 2004). It possibly corresponds to Phase 1 of Event 1 in Table S1. However, for subsequent failures (Phases 2-4 of Event 1), failure masses were deposited on the angular debris and boulders of the previous colluvium, characterized by a rough ground surface, resulting in lower mobility (Fig. 12d). This process of retrogression may be captured in the video (Fig. S2). Therefore, the most plausible landslide activities could be retrogression in Event 1. Then, the widening activity developed by toppling and rockfalls with subsequent Event 2, Event 3, and other failures from the steep scarp and flanks (Fig. 11) (refers to YouTube video: https://www.youtube.com/watch?v=PMlb7OiCqMQ; last access on 30 October 2024).

The continuous presence of the four phases in Event 1 (Fig. 4b) and the field survey imply a fractured bedrock/steep sliding surface near the CL. Following the landslide, steep scarps and flanks emerged, exhibiting discontinuities such as cleavage, joints, and numerous tension cracks at the crown (Figs. 9f-9j). This observation suggests the potential for further enlargement of the landslide. An unstable slope directly threatened the safety of residents living close to the crown of the CL. Therefore, it is imperative to implement comprehensive monitoring measures on the slopes described by Kang et al. (2021). These measures are essential for gaining a deeper understanding of ongoing landslide activity and ensuring the safety of the affected population.

444
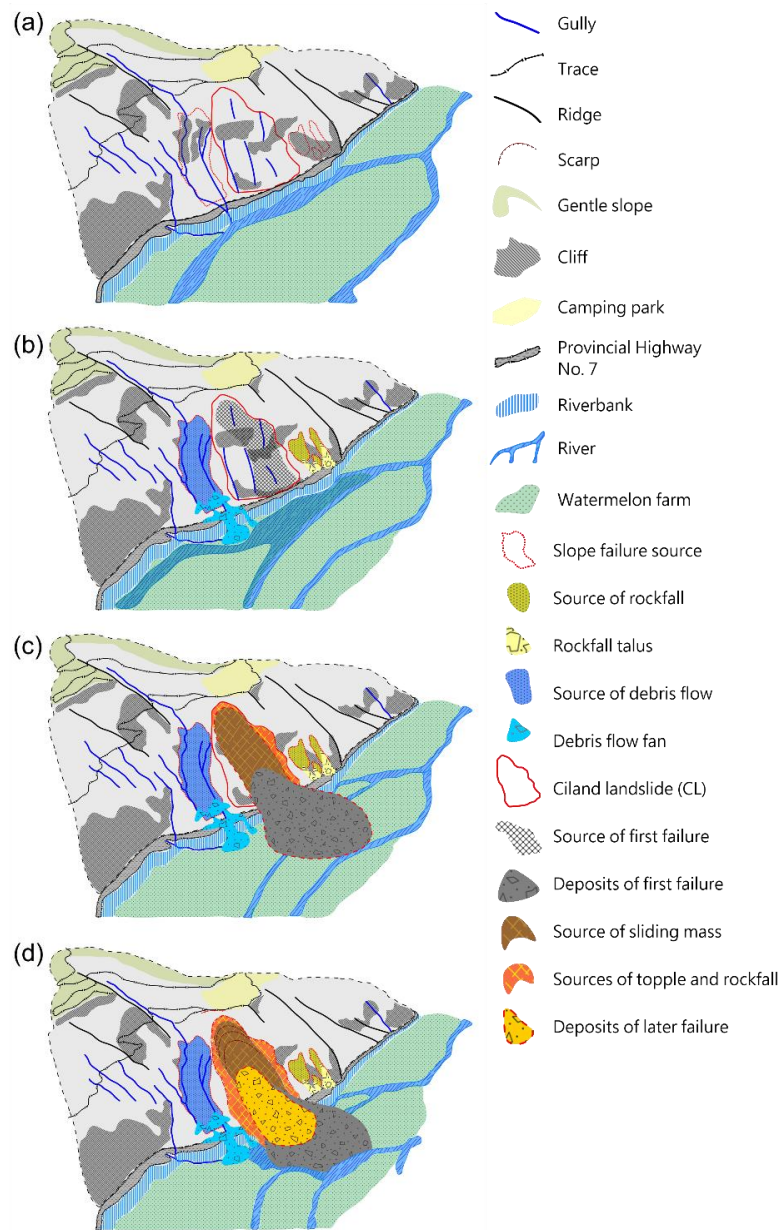
Figure 12 The geological model and topographic evolution of the CL. (a) The initial model is based on LiDAR topographic features. (b) According to Fig. 2 and Table S1, slope failures (debris flow and rockfalls) occurred around the CL. (c) The failure process of Phase 1 of Event 1 of the CL is based on Figs. 4 and 7 and Table 1. (d) The final stage of the CL, after Phases 2-4 of Event 1, Events 2 and 3 of the CL.

5.4 Future Perspective

The research demonstrates that seismic signal analysis provides geologists with timely information prior to field surveys, which is important in Taiwan. As a narrow island, Taiwan relies heavily on its provincial highways, especially the cross-island routes, for transportation. When landslides block these roads, the Highway Bureau of Taiwan must quickly remove the debris to reopen the routes. As a result, the post-landslide topography often changes during these engineering activities. In this study, for example, the field survey was conducted three days after the CL, by which time excavators had already altered some of the post-landslide deposits (Figure 8). Although seismic analysis has limitations in providing precise sliding direction, volume estimation, and understanding the physical process (Gualtieri and Ekström, 2018; Li et al., 2018; Chang et al., 2024), it offers sufficient preliminary information to assess the landslide's characteristics before more detailed fieldwork.

Looking ahead to medium and small landslide monitoring, high-frequency seismic signal analysis (>1 Hz) yields similar results, except for sliding direction, which remains challenging to determine. This limitation arises from the development of high-frequency Green's functions used to examine the force mechanism. Consequently, both low- and high-frequency seismic analysis algorithms can be flexibly applied depending on the monitoring objectives. Chang et al. (2024) have addressed relevant applications of this approach.

Additionally, during a seasonal inspection on May 27, 2022, prior to the CL, the downslope concrete wall was found to be slightly damaged and displaced (Figs. 9a-9e). This highlights the importance of regular roadside slope inspections. To face a similar situation in the future, techniques such as seismic ambient noise analysis (Colombero et al., 2021; Le Breton et al., 2021) and remote monitoring systems (Squarzoni et al., 2020) can be considered for long-term surveillance. The CL also caused numerous crown cracks (Figs. 9f-9j), posing additional risks of further failures that threaten the safety of residents living upslope. Comprehensive monitoring is, therefore, essential to better understand ongoing landslide activity and mitigate future risks (Kang et al., 2021).

6. Conclusions

Research on the Cilan Landslide (CL) has shown how to deliver seismic analysis results as pre-survey knowledge to geologists for field surveys. We investigated a series of events involving the efficient generation of one-hour spectrograms through a discrete Fourier transform. Three events, Event 1, Event 2, and Event 3, were identified, with four continuous phases of sliding, rockfall, and the subsequent toppling and rockfalls, as revealed by the spectrograms obtained via a Stockwell transform with a semi-log frequency axis. The initial sliding of the CL generated low-frequency seismic signals (ranging from 0.02 Hz to 0.05 Hz), and we successfully determined an inverted single force direction of 153.67°, close to the actual direction of landslide movement, which was 148°. This geohazard location (GeoLoc) pinpointed Event 1 and Event 2 close to seismic station V03G, whereas a polarization analysis provided further support for the notion that these event sources may have originated from the same direction, indicating a high probability of sharing the same slope of origin. Additionally, by employing the force magnitude and amplitude at the source (A_0) in the empirical regressions for Event 1 and Event 2 of the CL, we estimated the landslide volume to be 540,331 m^3, 19% lower than the volume calculated using a digital elevation model.

This information has significantly contributed to geologists' understanding of the physical processes underlying the CL for predicting advancing, retrogressive, enlarging, or widening mechanisms. After combining the field survey, the seismic analysis results have led geologists to propose a detailed mechanism for the CL. This mechanism involves shear-off from the roadside slope and subsequent mass sliding triggered by high pore-water pressure from rainfall infiltration. The observed physical behaviors of subsequent failures and topographic features with imbrication-like deposits suggest that the most plausible landslide activity may undergo retrogression and widening over time.

The research supported the idea that seismic analysis enables the determination of a landslide's inverted-force direction, estimated landslide volume, and physical processes. Notably, seismic analysis from an adjacent station provides additional temporal insight into landslides' dynamics, whereas geological surveys can only investigate the topography post-landslide to constrain the failure mechanisms. Therefore, seismic analysis provides crucial information for geologists before conducting field surveys.

Data availability

Waveform data for this study were provided by the Broadband Array in Taiwan for Seismology (BATS; https://doi.org/10.7914/SN/TW, Academia Sinica, Institute of Earth Sciences, 1996.) and the Central Weather Administration, Taiwan (CWA; https://doi.org/10.7914/SN/T5). The raw seismic data of V03G is available through Figshare (https://doi.org/10.6084/m9.figshare.24464281.v1). The digital terrain model (DTM) of the 20-meter resolution used in Fig. 2 is available from the Government Open Data Platform, Taiwan (https://data.gov.tw/dataset/35430; Ministry of the Interior, 2024). The road shape files are available from the National Land Surveying and Mapping Center, Taiwan (http://maps.nlsc.gov.tw/S_Maps/wms). The last accessed of all URLs was on 30 October 2024.

Competing interests

The contact author has declared that none of the authors has competing interests.

Author contribution

JM and CM conceived of the presented idea and wrote the manuscript. WA supervised the project, provided critical feedback, and helped shape the research, analysis, and manuscript. JM, CM, WA, and MW carried out the field investigations. CS, MW, TC, and CY discussed the results and contributed to the final manuscript.

Acknowledgments

The authors acknowledged the National Science and Technology Council of Taiwan (NSTC) for the funding support. The authors acknowledge the Forestry and Nature Conservation Agency, Taiwan for providing LiDAR data and the Geological Survey and Mining Management Agency, Taiwan for LiDAR data establishment. We also acknowledged the editor, Dr. Daniele Giordan, and two reviewers's feedback, which greatly improved the paper's quality.

Financial support

This study is financially supported by the National Science and Technology Council of Taiwan (NSTC) for Che-Ming Yang under grants NSTC 110-2116-M-239-001-MY2, NSTC 112-2116-M-239-001, NUU project No. SM113004 and We-An Chao under grants NSTC 111-2625-M-A49-004-MY3.

References

Agliardi, F., Crosta, G., and Zanchi, A.: Structural constraints on deep-seated slope deformation kinematics, Eng. Geol., 59(1-2), 83-102, https://doi.org/10.1016/S0013-7952(00)00066-1, 2001.

Aki, K. and Ferrazzini, V.: Seismic monitoring and modeling of an active volcano for prediction, J. Geophys. Res., 105, 16617–16640, https://doi.org/10.1029/2000JB900033, 2000.

Allstadt, K.: Extracting source characteristics and dynamics of the August 2010 Mount Meager landslide from broadband seismograms, J. Geophys. Res., 118, 1472–1490, https://doi.org/10.1002/jgrf.20110, 2013.

Brodsky, E. E., Gordeev, E., and Kanamori, H.: Landslide basal friction as measured by seismic waves, Geophys. Res. Lett., 30, 2236, https://doi.org/10.1029/2003GL018485, 2003.

Chang, J.M., Chao, W.A., Chen, H., Kuo, Y.T., and Yang, C.M.: Locating rock slope failures along highways and understanding their physical processes using seismic signals, Earth Surf. Dynam., 9, 505–517, https://doi.org/10.5194/esurf-9-505-2021, 2021.

Chang, J.M., Chao, W.A., Kuo, Y.T., Yang, C.M., Chen, H., and Wang, Yu.: Field experiments: How well can seismic monitoring assess rock mass falling? Eng. Geol., 323, 107211, https://doi.org/10.1016/j.enggeo.2023.107211, 2023.

Chang, J. M., Kuo, Y. T., Chao, W. A., Lin, C. M., Lan, H. W., Yang, C. M., & Chen, H.: Landslide Warning Area Delineation through Seismic Signals and Landslide Characteristics: Insights from the Silabaku Landslide in Southern Taiwan. Seismol. Res. Lett., 95(5), 2986-2996, https://doi.org/10.1785/0220230396, 2024.

Chao, W.A., Zhao, L., Chen, S.C., Wu, Y.M., Chen, C.H., and Huang, H.H.: Seismology-based early identification of dam-formation landquake events, Sci. Rep., 6, 19259, https://doi.org/10.1038/srep19259, 2016.

Chao, W.A., Wu, Y.M., Zhao, L., Chen, H., Chen, Y.G., Chang, J.M., and Lin, C.M.: A first near real-time seismology-based landquake monitoring system, Sci. Rep., 7, 43510, https://doi.org/10.1038/srep43510, 2017.

Chao, W.A., Wu, T.R., Ma, K.F., Kuo, Y.T., Wu, Y.M., Zhao, L., Chung, M.J., Wu, H., and Tsai, Y.L.: The large Greenland landslide of 2017: Was a tsunami warning possible? Seismol. Res. Lett. 89(4), 1335-1344. https://doi.org/10.1785/0220170160, 2018.

Chen, C.-H., Chao, W.A., Wu, Y.M., Zhao, L., Chen, Y.G., Ho, W.Y., Lin, T.L., Kuo, K.H., and Chang, J.M.: A seismological study of landquakes using a real-time broad-band seismic network, Geophys. J. Int., 194, 885–898, https://doi.org/10.1093/gji/ggt121, 2013.

Chen, L.C.: Action Plan for Prevention and Control of Large-Scale Landslide Disasters (In Chinese), National Science and Technology Center for Disaster Reduction, Taiwan, https://reurl.cc/M8anXL, 2015.

Chigira, M.: Long-term gravitational deformation of rocks by mass rock creep. Eng. Geol., 32, 157-184, https://doi.org/10.1016/0013-7952(92)90043-X, 1992.

Colombero, C., Jongmans, D., Fiolleau, S., Valentin, J., Baillet, L., & Bièvre, G.: Seismic noise parameters as indicators of reversible modifications in slope stability: a review. Surveys in Geophysics, 42, 339-375, https://doi.org/10.1007/s10712-021-09632-w, 2021.

Cooper, R.G. 2007. Mass Movements in Great Britain, Geological Conservation Review Series, No. 33, Joint Nature Conservation Committee, Peterborough, 348 pp.

Dammeier, F., Moore, J.R., Haslinger, F. and S. Loew: Characterization of alpine rockslides using statistical analysis of seismic signals, J. Geophys. Res., 116, F04024, https://doi:10.1029/2011JF002037, 2011.

Dietze, M., Turowski, J. M., Cook, K. L., and Hovius, N.: Spatiotemporal patterns, triggers and anatomies of seismically detected rockfalls, Earth Surf. Dynam., 5, 757–779, https://doi.org/10.5194/esurf-5-757-2017, 2017.

Ekström, G. and Stark, C. P.: Simple scaling of catastrophic landslide dynamics, Science, 339, 1416–1419, https://doi:10.1126/science.1232887, 2013.

Fei, L.Y., Chen, M.M.: Geological investigation and database construction for upstream of flood-prone area – maps and explanatory text (In Chinese). Central Geological Survey, MOEA, Taiwan, 192, 2013.

Feng, Z.: The seismic signatures of the 2009 Shiaolin landslide in Taiwan, Nat. Hazards Earth Syst. Sci., 11, 1559–1569, https://doi.org/10.5194/nhess-11-1559-2011, 2011.

Fuchs, F., Lenhardt, W., Bokelmann, G., and the AlpArray Working Group: Seismic detection of rockslides at regional scale: examples from the Eastern Alps and feasibility of kurtosis-based event location, Earth Surf. Dynam., 6, 955–970, https://doi.org/10.5194/esurf-6-955-2018, 2018.

Guinau, M., Tapia, M., Pérez-Guillén, C., Suriñach, E., Roig, P., Khazaradze, G., Torné, M., Royán, M. J., and Echeverria, A.: Remote sensing and seismic data integration for the characterization of a rock slide and an artificially triggered rock fall, Eng. Geol., 257, 105113, https://doi.org/10.1016/j.enggeo.2019.04.010, 2019.

Gualtieri, L., and Ekström, G.: Broad-band seismic analysis and modeling of the 2015 Taan Fjord, Alaska landslide using Instaseis. Geophysical Journal International, 213(3), 1912-1923, https://doi.org/10.1093/gji/ggy086, 2018.

Hibert, C., Ekström, G., and Stark, C. P.: Dynamics of the Bingham Canyon Mine landslides from seismic signal analysis, Geophys. Res. Lett., 41, 4413-4804, https://doi.org/10.1002/2014GL060592, 2014.

Hibert, C., Stark, C. P., and Ekström, G.: Dynamics of the Oso-Steelhead landslide from broadband seismic analysis, Nat. Hazards Earth Syst. Sci., 15, 1265–1273, https://doi.org/10.5194/nhess-15-1265-2015, 2015.

Hungr, O., and Evans, S.G.: Entrainment of debris in rock avalanches: An analysis of a long run-out mechanism. GSA Bulletin, 116 (9-10), 1240–1252. https://doi.org/10.1130/B25362.1, 2004.

Hungr, O., Leroueil, S., and Picarelli, L.: The Varnes classification of landslide types, an update. Landslides 11, 167–194, https://doi.org/10.1007/s10346-013-0436-y, 2014.

Kanamori, H., and Given, J. W.: Analysis of long-period seismic waves excited by the May 18, 1980, eruption of Mount St. Helens - A terrestrial monopole?, J. Geophys. Res., 87, 5422–5432, doi:10.1029/JB087iB07p05422, 1982.

Kang, K.H., Chao, W.A., Yang, C.M., Chung, M.C., Kuo, Y.T., Yeh, C.H, Liu, H.C., Lin, C.H., Lin, C.P., Liao, J.J., Chang, J.M., Ngui, Y.N., and Tai, T.L.: Rigidity Strengthening of Landslide Materials Measured by Seismic Interferometry. Remote Sens. 13(14), 2834. https://doi.org/10.3390/rs13142834, 2021.

Kao, H., Jian, P.R., Ma, K.F., Huang, B.S. and Liu, C.C.: Moment-tensor inversion for offshore earthquakes east of Taiwan and their implications to regional collision. Geophys. Res. Lett., 25, 3619-3622. https://doi.org/10.1029/98GL02803, 1998.

Kuo, H.L., Lin, G.W., Chen, C.W., Saito, H., Lin, C.W., Chen, H., and Chao, W.A.: Evaluating critical rainfall conditions for large-scale landslides by detecting event times from seismic records, Nat. Hazards Earth Syst. Sci., 18, 2877–2891, https://doi.org/10.5194/nhess-18-2877-2018, 2018.

Le Breton, M., Bontemps, N., Guillemot, A., Baillet, L., & Larose, É.: Landslide monitoring using seismic ambient noise correlation: challenges and applications. Earth-Science Reviews, 216, 103518, https://doi.org/10.1016/j.earscirev.2021.103518, 2021.

Legros, F.: The Mobility of Long-Runout Landslides. Eng. Geol., 63, 301-331. http://dx.doi.org/10.1016/S0013-7952(01)00090-4, 2002.

Li, W., Zhang, Y., Xu, Y., Zheng, X., Wang, R., Su, J., Yi, G., and Huang, Q.: Complex dynamics of repeating and river-blocking landslides in Jiangda during 2018, Earthq. Sci., 34(1), https://doi.org/10.29382/eqs-2020-0034, 3-14, 2021.

Manconi, A., Mondini, A. C., and the AlpArray working group: Landslides caught on seismic networks and satellite radars, Nat. Hazards Earth Syst. Sci., 22, 1655–1664, https://doi.org/10.5194/nhess-22-1655-2022, 2022.

Moretti, L., Mangeney, A., Capdeville, Y., Stutzmann, E., Huggel, C., Schneider, D., and Bouchut, F.: Numerical modeling of the mount Steller landslide flow history and of the generated long period seismic waves. Geophys. Res. Lett., 39, L16402, https://doi.org/10.1029/2012GL052511, 2012.

Provost, F., Malet, J.-P., Hibert, C., Helmstetter, A., Radiguet, M., Amitrano, D., Langet, N., Larose, E., Abancó, C., Hürlimann, M., Lebourg, T., Levy, C., Le Roy, G., Ulrich, P., Vidal, M., and Vial, B.: Towards a standard typology of endogenous landslide seismic sources, Earth Surf. Dynam., 6, 1059-1088, https://doi.org/10.5194/esurf-6-1059-2018, 2018.

Sassa, K.: Landslide volume–apparent friction angle relationship in the case of rapid loading on alluvial deposits. Landslide News 6, 16 – 19, 1992.

Shin, T.C., and Chen, Y.L.: Study of earthquake location of 3-D velocity structure in Taiwan area. (In Chinese). Meteorological Bulletin 42, 135-169, https://photino.cwb.gov.tw/rdcweb/lib/cd/cd07mb/MB/PDF/42/No.2/03.pdf,1998.

Squarzoni, G., Bayer, B., Franceschini, S., and Simoni, A.: Pre-and post-failure dynamics of landslides in the Northern Apennines revealed by space-borne synthetic aperture radar interferometry (InSAR). Geomorphology, 369, 107353, https://doi.org/10.1016/j.geomorph.2020.107353, 2020.

Suriñach, E., Vilajosana, I., Khazaradze, G., Biescas, B., Furdada, G., and Vilaplana, J. M.: Seismic detection and characterization of landslides and other mass movements, Nat. Hazards Earth Syst. Sci., 5, 791–798, https://doi.org/10.5194/nhess-5-791-2005, 2005.

Varnes, D.: Slope movement types and processes. In Landslides: Analysis and Control (eds Schuster, R. L. & Krizek, R. J.), Transportation Research Board, National Academy of Science, Washington, 1978.

Vilajosana, I., Suriñach, E., Abellán, A., Khazaradze, G., Garcia, D., and Llosa, J.: Rockfall induced seismic signals: case study in Montserrat, Catalonia, Nat. Hazards Earth Syst. Sci., 8, 805–812, https://doi.org/10.5194/nhess-8-805-2008, 2008.

Walter, F., Burtin, A., McArdell, B. W., Hovius, N., Weder, B., and Turowski, J. M.: Testing seismic amplitude source location for fast debris-flow detection at Illgraben, Switzerland, Nat. Hazards Earth Syst. Sci., 17, 939–955, https://doi.org/10.5194/nhess-17-939-2017, 2017.

Walsh, B., Jolly, A. D., and Procter, J.: Calibrating the amplitude source location (ASL) method by using active seismic sources: An example from Te Maari volcano, Tongariro National Park, New Zealand, Geophys. Res. Lett., 44, 3591–3599, https://doi.org/10.1002/2017GL073000, 2017.

Weng, M.C., Lin, C.H., Shiu, W.J., Chao, W.A., Chiu, C.C., Lee, C.F., Huang, W.K., and Yang, C.M.: Towards a rapid assessment of highway slope disasters by using multidisciplinary techniques, Landslides, 19, 687–701, https://doi.org/10.1007/s10346-021-01808-0, 2022.

WP/ WLI. (International Geotechnical Societies UNESCO Working Party on World Landslide Inventory) 1993. A suggested method for describing the activity of a landslide. Bull. Eng. Geol., No. 47, 53-57.

Wu, Y.M., Chang, C.H., Zhao, L., Shyu, J.B.H., Chen, Y.G., Sieh, K., and Avouac, J.P.: Seismic tomography of Taiwan: improved constraints from a dense network of strong-motion stations, J. Geophys. Res.: Solid Earth, 112, B08312, https://doi:10.1029/2007JB004983, 2007.

Yamada, M., Kumagai, H., Matsushi, Y., and Matsuzawa, T.: Dynamic landslide processes revealed by broadband seismic records, Geophys. Res. Lett., 40, 2998–3002, doi:10.1002/grl.50437, 2013.

Yang, C.M., Chang, J.M., Hung, C.Y., Lu, C.H., Chao, W.A. and Kang, K.H.: Life span of a landslide dam on mountain valley caught on seismic signals and its possible early warnings, Landslides, 19, 637–646, https://doi.org/10.1007/s10346-021-01818-y, 2022.